JACS
JOURNAL OF THE AMERICAN CHEMICAL SOCIETY
Article
pubs.acs.org/JACS

# In Situ X-ray Absorption Spectroscopy Investigation of a Bifunctional Manganese Oxide Catalyst with High Activity for Electrochemical Water Oxidation and Oxygen Reduction

Yelena Gorlin,[†] Benedikt Lassalle-Kaiser,[‡] Jesse D. Benck,[†] Sheraz Gul,[‡] Samuel M. Webb,[§] Vittal K. Yachandra,[‡] Junko Yano,*[,‡] and Thomas F. Jaramillo*[,†]

[†]Department of Chemical Engineering, Stanford University, Stanford, California 94305, United States
[‡]Physical Biosciences Division, Lawrence Berkeley National Laboratory, Berkeley, California 94720, United States
[§]Stanford Synchrotron Radiation Lightsource, SLAC National Accelerator Laboratory, Menlo Park, California 94025, United States

Supporting Information

**ABSTRACT:** In situ X-ray absorption spectroscopy (XAS) is a powerful technique that can be applied to electrochemical systems, with the ability to elucidate the chemical nature of electrocatalysts under reaction conditions. In this study, we perform in situ XAS measurements on a bifunctional manganese oxide ($MnO_x$) catalyst with high electrochemical activity for the oxygen reduction reaction (ORR) and the oxygen evolution reaction (OER). Using X-ray absorption near edge structure (XANES) and extended X-ray absorption fine structure (EXAFS), we find that exposure to an ORR-relevant potential of 0.7 V vs RHE produces a disordered $Mn_3^{II,III,III}O_4$ phase with negligible contributions from other phases. After the potential is increased to a highly anodic value of 1.8 V vs RHE, relevant to the OER, we observe an oxidation of approximately 80% of the catalytic thin film to form a mixed $Mn^{III,IV}$ oxide, while the remaining 20% of the film consists of a less oxidized phase, likely corresponding to unchanged $Mn_3^{II,III,III}O_4$. XAS and electrochemical characterization of two thin film catalysts with different $MnO_x$ thicknesses reveals no significant influence of thickness on the measured oxidation states, at either ORR or OER potentials, but demonstrates that the OER activity scales with film thickness. This result suggests that the films have porous structure, which does not restrict electrocatalysis to the top geometric layer of the film. As the portion of the catalyst film that is most likely to be oxidized at the high potentials necessary for the OER is that which is closest to the electrolyte interface, we hypothesize that the $Mn^{III,IV}$ oxide, rather than $Mn_3^{II,III,III}O_4$, is the phase pertinent to the observed OER activity.

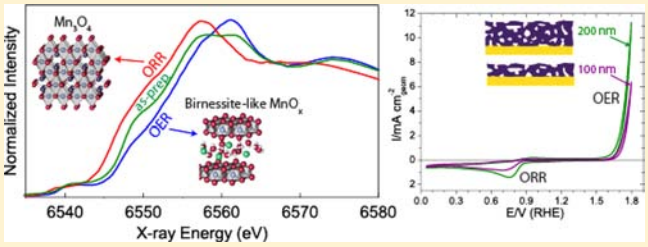


## INTRODUCTION

The development of catalytic materials for the oxygen reduction reaction (ORR) and the oxygen evolution reaction (OER) is one of the major challenges in electrochemical energy conversion and storage technologies such as fuel cells, metal–air batteries, electrolysis cells, and solar fuel synthesis reactors. To implement strategies for the rational design of catalysts for the ORR and the OER, it is important to improve understanding of the chemical state and structure of active surfaces under reaction conditions. X-ray absorption spectroscopy (XAS) can be combined with electrochemistry to elucidate the properties of catalytic materials in situ. X-ray absorption near edge structure (XANES) probes the electronic structure of the catalyst, while the extended X-ray absorption fine structure (EXAFS) probes the bond geometry and coordination of the catalysts. In the past, in situ XAS measurements have been applied to a variety of ORR and OER catalyst systems. For example, in situ XAS measurements have been used to track the oxidation state of platinum as a function of potential in the ORR region,[1] correlate d-band vacancies on platinum alloy catalysts to oxygen reduction activity,[2] and link higher $Mn^{IV}O_2$ content to better ORR performance in $MnO_x$ catalysts.[3,4] The method has also been used to understand the valency and structure of cobalt phosphate and nickel borate OER catalysts[5,6] and investigate photochemical oxygen evolution on a tetranuclear manganese cluster.[7]

Only a few in situ XAS studies, however, have described changes in the active catalyst phase between the ORR and OER regimes using the same material.[8] The significant overpotentials associated with these two reactions make it unlikely that the same surface phase will form under both reductive and oxidative potentials.[9] Because of the large number of $MnO_x$ phases that may be associated with high ORR[4,10−13] and OER activities,[14−16] it could be possible for $MnO_x$-based catalysts to change surface structure as a function of potential and still exhibit high activity for both reactions. In our work, we performed in situ XAS measurements on a bifunctional manganese oxide ($MnO_x$) catalyst with high electrochemical

**Received:** November 6, 2012
**Published:** June 3, 2013

   dx.doi.org/10.1021/ja3104632 | J. Am. Chem. Soc. 2013, 135, 8525−8534

activity for both the ORR and the OER. To prepare a bifunctional $MnO_x$ catalyst, we adopted a synthesis procedure previously developed for the deposition of $MnO_x$ on glassy carbon (GC)[13] to deposition on a gold-coated silicon nitride ($Au-Si_3N_4$) window. Using information from in situ XANES and EXAFS, we found that the switch from ORR to OER potentials results in a structural change in the $MnO_x/Au-Si_3N_4$ catalyst and characterized the $MnO_x$ phases present under each set of conditions. We also studied samples with two different thicknesses of the catalytic layer to investigate the porosity and electrochemical accessibility of the $MnO_x$ films. Our results link specific Mn oxide phases to ORR and OER conditions, thus increasing understanding of oxygen electrocatalysis on $MnO_x$ electrodes.

## EXPERIMENTAL SECTION

**Electrodeposition of Manganese Oxide Catalyst.** Prior to manganese oxide ($MnO_x$) electrodeposition, silicon nitride membrane ($Si_3N_4$) windows (1000 nm membrane, Silson Ltd.) were sputter-coated with a 10 nm binding layer of titanium and a 100 nm layer of gold to produce a suitable electrode substrate ($Au-Si_3N_4$). The catalyst was synthesized via a previously reported procedure.[13,17] The electrolyte used for deposition was prepared by dissolving 0.71 g of sodium sulfate (Sigma-Aldrich, >99.0%) and 1.23 g of manganous acetate (Aldrich, 99.99%) in 50 mL of Millipore water at room temperature, yielding a solution with pH of 7.4. The solution was then aged for 6 days, until the pH dropped to approximately 7. Manganese oxide was electrodeposited in a three electrode electrochemical cell using the $Au-Si_3N_4$ substrate contacted by copper tape as the working electrode, a Ag|AgCl reference electrode, and a graphite foil counter electrode. Before performing the electrodeposition, the resistance between the working and reference electrodes was measured to ensure proper electrical contact between copper tape and the gold layer of $Au-Si_3N_4$. After establishing a proper contact and achieving a resistance of 30–60 Ω, the potential was *iR* compensated to 85% and cycled nine times between 0.0 and 0.6 V vs Ag|AgCl at a sweep rate of 20 $mV \cdot s^{-1}$. The $Au-Si_3N_4$ membrane coated with the resulting thin film was placed in a ceramic boat (Fisher Scientific) and heat treated in air at 480 °C for 10 h in a tube furnace (Mellen Company SC13).

**Electrochemical Characterization.** The electrochemical activity of the electrodeposited $MnO_x$ thin film was first evaluated using cyclic voltammetry in a three-electrode electrochemical cell. All cyclic voltammograms (CVs) were *iR*-compensated to 85% and measured in 0.1 M KOH electrolyte at 23 °C with a sweep rate of 20 $mV \cdot s^{-1}$, using a carbon rod counter electrode and a Ag|AgCl reference electrode. The electrolyte (0.1 M KOH) was prepared from high purity KOH pellets (Sigma-Aldrich, 99.99%) by adding 5.60 g of pellets to 1 L of Millipore water. The potential scale was calibrated to a reversible hydrogen electrode (RHE) at the end of the catalyst characterization in a hydrogen saturated electrolyte with platinum nanoparticles as the working electrode (20 wt % Pt on Vulcan XC-72, Etek). The potential of 0.960 V at which the current crossed zero was taken to be the thermodynamic potential for the hydrogen electrode reactions. All potentials during electrochemical characterization are reported vs RHE. To characterize the activity of the catalyst for the oxygen evolution reaction (OER) and the oxygen reduction reaction (ORR), CVs were performed over a potential range of 0.05–1.8 V in an oxygen saturated environment. Additional CVs were performed from 0.05 to 1.1 V in oxygen and nitrogen saturated environments to confirm the electrocatalytic activity of the catalyst for the ORR.

**Physical Characterization.** The morphology of the $MnO_x$ catalyst was studied using scanning electron microscopy (SEM, FEI Magellan 400 XHR). A 25 pA beam current of 5 kV and a secondary electron detector were used. The crystal structure of $MnO_x$ catalyst was investigated using X-ray diffraction with Cu K$\alpha$1 radiation and $\lambda$ = 1.54 Å, operated at 45 kV and 40 mA (XRD, Phillips X'Pert 2). $2\theta$ scans from 10° to 90° were performed on the catalyst and the bare $Au-Si_3N_4$ substrate, at a scan speed of 0.02 $deg \cdot s^{-1}$.

**Ex Situ XPS Characterization.** The manganese oxidation state and potassium intercalation were studied by X-ray photoelectron spectroscopy (XPS) using monochromated Al K$\alpha$ 1486.6 eV X-rays (XPS, PHI 5000 VersaProbe). Three samples were investigated: an as-prepared sample, an ORR relevant sample, and an OER relevant sample. To prepare the ORR and OER relevant samples, $MnO_x$ on $Au-Si_3N_4$ was cycled from 0.05 V vs RHE to a vertex potential of either 0.70 or 1.8 V vs RHE, held at the vertex potential for 10 min, extracted from the electrochemical cell under potential control, and characterized using XPS. During the ex situ XPS characterization, the high-resolution spectra in Mn 2p, Mn 3s, and C 1s/K 2p regions were obtained on the $MnO_x$ catalysts, and four powder standards: $Mn^{II}O$, $Mn_3^{II,III,III}O_4$, $Mn_2^{III}O_3$, and $Mn^{IV}O_2$ (Sigma-Aldrich). $Mn_3^{II,III,III}O_4$, $Mn_2^{III}O_3$, and $Mn^{IV}O_2$ powders were used as received, while $Mn^{II}O$ powder was sputtered prior to collecting XPS spectra to remove the oxidized surface known to form on $Mn^{II}O$ in air.[18] All spectra were collected using a pass energy of 23.5 eV, an energy step of 0.1 eV, and a time of 20 ms per step and were calibrated to the position of adventitious carbon at 285.0 eV.[19] The specific energy windows and the number of scans used to acquire each high resolution spectrum are provided in Table S1. Details describing XPS data analysis are provided in the Supporting Information (SI). To monitor changes in the Mn oxidation state of $MnO_x$ catalyst, we looked at the distance between Mn $2p_{1/2}$ peak and its satellite ($\Delta 2p_{1/2}$) and the magnitude of the Mn 3s multiplet splitting ($\Delta$E3s), which have been previously shown to either increase ($\Delta 2p_{1/2}$) or decrease ($\Delta$E3s) with increasing Mn oxidation state in powder standards.[20,21] This trend is especially clear when using $Mn^{II}O$, $Mn_2^{III}O_3$, and $Mn^{IV}O_2$ powders, representing $Mn^{II}$, $Mn^{III}$, and $Mn^{IV}$ oxidation states, while inclusion of additional phases, such as $Mn_3^{II,III,III}O_4$, does not offer a greater ability to discriminate between the oxidation states.[21,22] The Mn 2p and the Mn 3s spectra of $Mn_3^{II,III,III}O_4$ are characterized by broader peaks, and its $2p_{1/2}$ satellite position falls between $Mn_2^{III}O_3$ and $Mn^{IV}O_2$, despite its lower oxidation state than that of either $Mn_2^{III}O_3$ or $Mn^{IV}O_2$.[20,21] For comparison we collected the spectra of $Mn_3^{II,III,III}O_4$ powder and present it alongside the other standards. In agreement with previous reports, we find that, for our catalyst samples, XPS alone is not sufficient to distinguish between the $Mn_2^{III}O_3$ and $Mn_3^{II,III,III}O_4$ phases.

**In Situ Mn K-Edge XAS.** X-ray absorption spectra (XAS) were collected at the Advanced Light Source (ALS) on beamline 10.3.2[23] with an electron energy of 1.9 GeV and an average current of 500 mA. The radiation was monochromatized by a Si (111) double-crystal monochromator. The intensity of the incident X-ray was monitored by an $N_2$-filled ion chamber ($I_0$) in front of the sample. Fluorescence spectra were recorded using a seven-element Ge solid-state detector. For electrochemical experiments, no transmission data could be collected. The energy was therefore calibrated using a glitch in the $I_0$ relative to the absorption edge of Mn foil, as is commonly employed in XAS experiments. All data were collected at room temperature. Data reduction of the XAS spectra was performed using custom-made software. Pre-edge and post-edge contributions were subtracted from the XAS spectra, and the results were normalized with respect to the edge jump. Background removal in *k*-space was achieved through a five-domain cubic spline. Curve fitting was performed with Artemis and IFEFFIT software using ab initio-calculated phases and amplitudes from the program FEFF 8.2.[24,25] The details of curve fitting are discussed in the SI. A schematic of the in situ setup is shown in Figure 1. In this setup, the back side of the $Si_3N_4$ window was exposed to X-rays, while the front side of the $Si_3N_4$ window with electrodeposited $MnO_x$ on Au/Ti layer faced into the interior of the electrochemical cell. Electrochemistry was performed using a Ag|AgCl reference electrode, a platinum wire counter electrode, and 0.1 M KOH electrolyte exposed to ambient air. Although RHE calibration was not performed during in situ XAS characterization, we assumed the same shift of 0.960 V for the Ag|AgCl reference electrode and report all potentials vs RHE. After preparing the electrochemical cell for in situ XAS measurements, the resistance between the working and reference electrodes was measured to ensure proper electrical contact between


dx.doi.org/10.1021/ja3104632 | J. Am. Chem. Soc. 2013, 135, 8525–8534

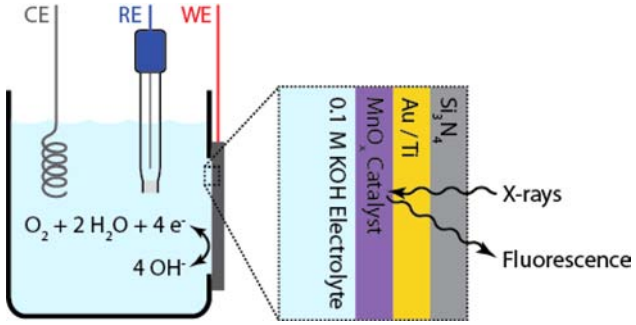


**Figure 1.** In situ XAS setup, with the back side of the $Si_3N_4$ window facing the X-rays and the front side of the window with electrodeposited $MnO_x$ on a layer of Au/Ti facing the electrolyte. CE, RE, and WE stand for counter, reference, and working electrodes, respectively.

the potentiostat and $MnO_x$ on Au−$Si_3N_4$. After achieving a resistance of 150 Ω, a CV was performed from 0.05 to 1.1 V to record the electrochemical features of the working electrode. During in situ XAS at ORR relevant conditions, the potential was held at 0.7 V for 3.4 h. After the completion of the measurement, the resistance between the working and reference electrodes was measured to be 73 Ω and *iR*-compensated cyclic voltammetry was performed from 0.05 to 1.8 V to record the bifunctional OER/ORR activity of the working electrode. During in situ XAS at OER relevant conditions, the *iR*-compensated potential was held at 1.8 V for 5 h. The solutions were not stirred during the measurements. After each potential change, the system was allowed to equilibrate for 5 min. Spectra were acquired in Quick-EXAFS (QXAS) mode. For the thick (nine cycles) samples, four sets of 20 spectra each lasting 3 min were recorded. For the thin samples (one cycle), 20 sets of 20 spectra that lasted 3 min each were recorded. No spectral changes were observed between the first and last spectrum of a series of 20 scans or between the first and last sets of spectra, as shown in Figures S1 and S2. Typical EXAFS spectra demonstrating the signal-to-noise for each electrochemical condition are provided in Figure S3.

The collected XAS spectra of $MnO_x$ on Au−$Si_3N_4$ were compared to ex situ XAS spectra of model $MnO_x$ compounds, including $Mn^{II}O$, $Mn_3^{II,III,III}O_4$, $\alpha$-$Mn_2^{III}O_3$, $\gamma$-$Mn^{III}OOH$, $\beta$-$Mn^{IV}O_2$, and $Mg^{2+}$ birnessite. $Mn^{II}O$ and $Mn_3^{II,III,III}O_4$ powders were obtained from Sigma-Aldrich and used as purchased. $\beta$-$Mn^{IV}O_2$ and $\alpha$-$Mn_2^{III}O_3$ phases were prepared by dissolving $Mn(NO_3)_2{\cdot}H_2O$ in water, drying the solution at 60 °C for 24 h, and calcining the powder for 3 h at 200 or 500 °C, respectively. $\gamma$-$Mn^{III}OOH$ powder was synthesized by preparing a solution consisting of 8 mM $MnSO_4$ and 8 mM $NH_4S_2O_8$, adjusting it to pH 10 using 1 M NaOH, and heating it in a sealed autoclave at 120 °C for 10 h; the resulting powder was then washed and dried under vacuum. Powder XRD was used to confirm the phase of each synthesized compound (Figure S4). The details of $Mg^{2+}$ birnessite synthesis and powder XRD characterization are described in a previously published study by Webb and co-workers.[26] Table S2 in the SI provides a summary of all the standards used in this work as well as other $MnO_x$ phases mentioned in the text.

## RESULTS AND DISCUSSION

**$MnO_x$/Au−$Si_3N_4$ Catalyst.** To investigate the material properties of an active manganese oxide ($MnO_x$) catalyst under reaction conditions, we prepared $MnO_x$ on a gold-coated silicon nitride membrane (Au−$Si_3N_4$) following a previously developed procedure for deposition of $MnO_x$ catalyst onto a glassy carbon (GC) support.[13] The resulting electrode, $MnO_x$/Au−$Si_3N_4$, exhibited the expected bifunctional activity for both oxygen evolution reaction (OER) and oxygen reduction reaction (ORR) in alkaline electrolyte. The OER activity was confirmed by the formation of visible oxygen bubbles on the electrode surface at high oxidizing potentials, while the ORR activity was confirmed by performing additional characterization in both nitrogen and oxygen saturated electrolytes, which showed a significant increase in the reductive current in the presence of oxygen (Figure S5). To verify that $MnO_x$ is the active species responsible for the OER and the ORR, we compared the catalytic activity of $MnO_x$/Au−$Si_3N_4$ to that of the bare support, Au−$Si_3N_4$ (Figure 2A). The catalyst clearly

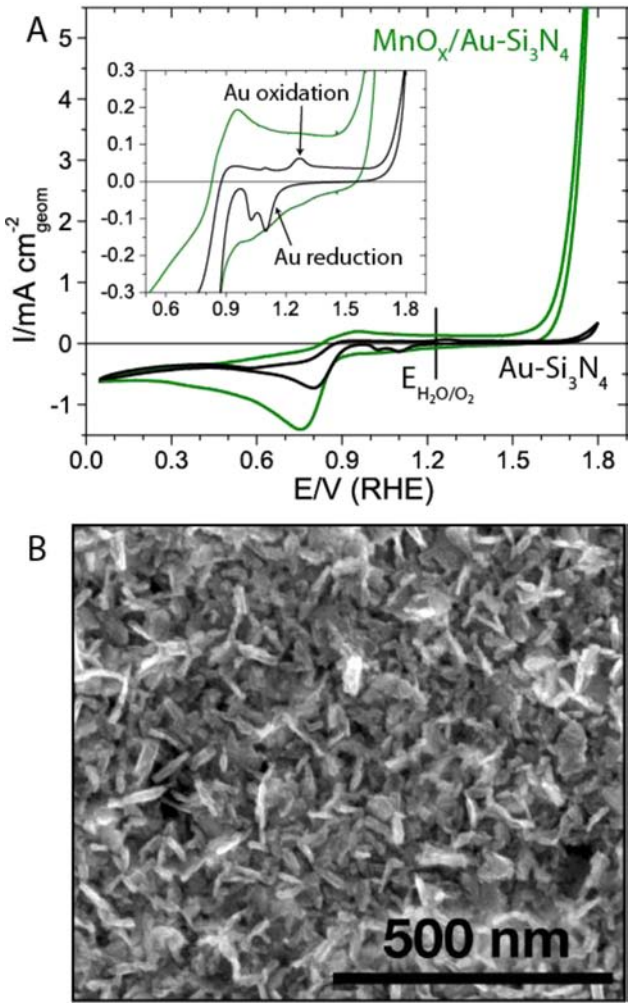


**Figure 2.** (A) Cyclic voltammetry of the $MnO_x$ catalyst in $O_2$ showing bifunctional ORR/OER activity and the background activity of the Au−$Si_3N_4$ support. Inset shows the disappearance of Au redox features after addition of $MnO_x$; (B) Scanning electron microscopy image illustrating needle-like morphology of $MnO_x$.

outperforms the bare gold support for the OER but demonstrates similar ORR activity to Au−$Si_3N_4$. To deconvolute the contributions from $MnO_x$ and Au in the observed ORR activity of the $MnO_x$/Au−$Si_3N_4$ catalyst, we examined the cyclic voltammograms of $MnO_x$/Au−$Si_3N_4$ and bare Au−$Si_3N_4$ in the potential region from 1.0 to 1.4 V, where gold oxidation and reduction features are prominent.[27] The electrochemical behavior of the electrodes, plotted in the inset of Figure 2A, demonstrates that the surface of the $MnO_x$/Au−$Si_3N_4$ catalyst does not display significant redox features characteristic of gold, indicating that the Au is electrochemically inaccessible. This finding links the observed ORR activity of $MnO_x$/Au−$Si_3N_4$ to the $MnO_x$ surface. The comparison of the


dx.doi.org/10.1021/ja3104632 | J. Am. Chem. Soc. 2013, 135, 8525−8534

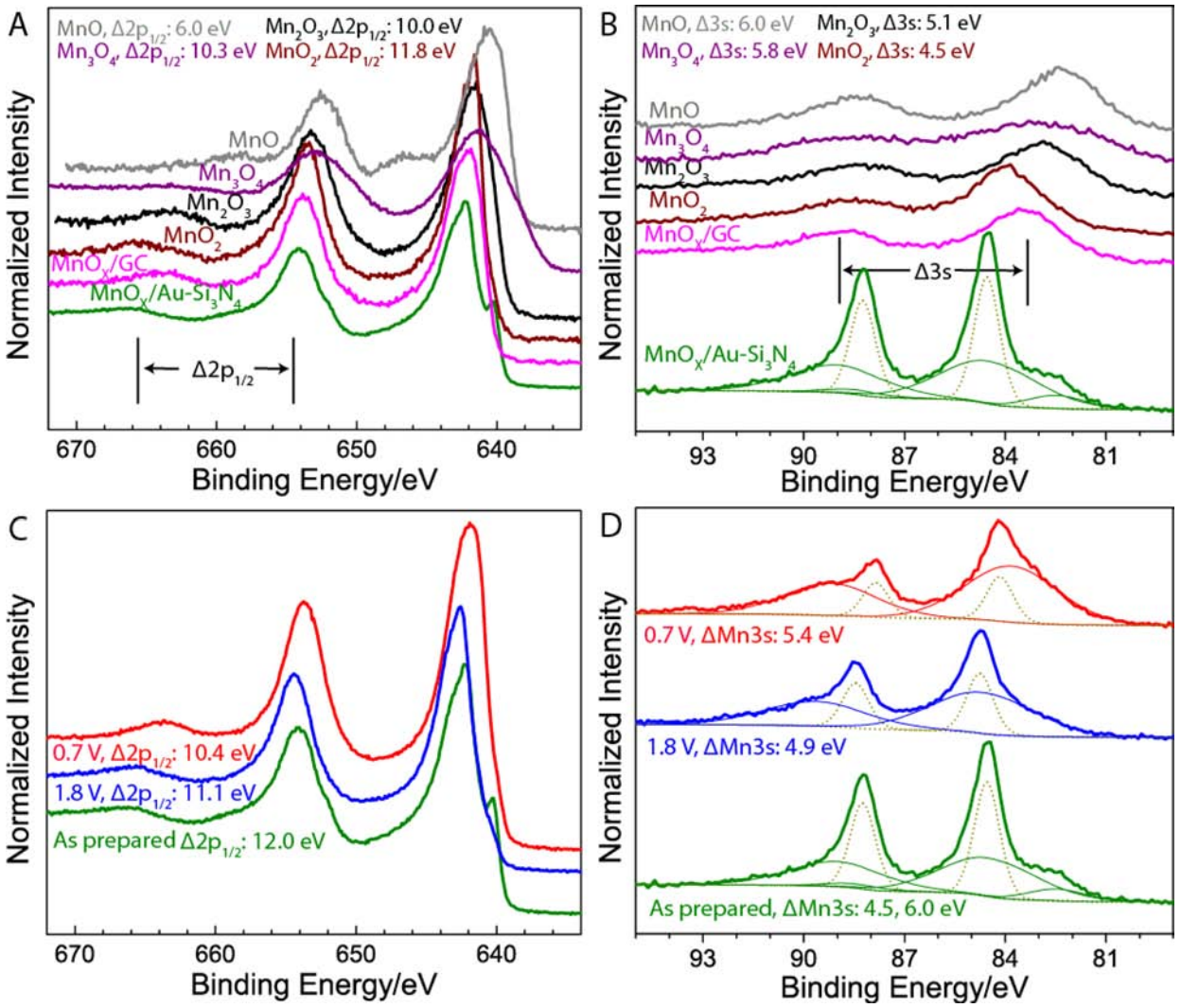


**Figure 3.** (A, B) Comparison of Mn 2p and Mn 3s spectra of $MnO_x$ on Au−$Si_3N_4$ and glassy carbon supports to the spectra of $MnO_2$, $Mn_2O_3$, $Mn_3O_4$, and MnO powder standards. (C, D) Comparison of Mn 2p and Mn 3s spectra of $MnO_x$ on Au−$Si_3N_4$ support to the spectra of the same sample after exposure to ORR or OER relevant potentials.

bifunctional oxygen electrode activity of $MnO_x$/Au−$Si_3N_4$ to the previously reported activity of $MnO_x$/GC (Figure S6) demonstrates that the two catalysts have similar catalytic activity when normalized to the geometric surface area.

Although the $MnO_x$/Au−$Si_3N_4$ exhibits similar activity to the $MnO_x$/GC studied previously, physical and chemical characterization illustrate that these materials have different properties. $MnO_x$/GC formed a nanostructured morphology with $\alpha$-$Mn_2^{III}O_3$ crystallinity.[13] $MnO_x$/Au−$Si_3N_4$, on the other hand, consists of densely packed needles, shown in Figure 2B, and has no long-range atomic order as demonstrated by the absence of the X-ray diffraction peaks in Figure S7.

**Ex Situ XPS.** The observed differences in the morphology and crystallinity of $MnO_x$/GC and $MnO_x$/Au−$Si_3N_4$ suggest that $MnO_x$/Au−$Si_3N_4$ might assume a different surface oxidation state than $MnO_x$/GC despite their identical preparation conditions. Previous ex situ XPS characterization of $MnO_x$/GC determined that the catalyst deposits as Mn(III) oxide[13] and that the possible changes to the surface oxidation state after an application of the ORR or the OER relevant potentials are too small to be detected by ex situ XPS.[28] Similar ex situ XPS characterization of the $MnO_x$/Au−$Si_3N_4$ surface shown in Figure 3 reveals important differences between $MnO_x$ deposited on Au−$Si_3N_4$ and GC. In Figure 3A, we compare the Mn 2p spectra of $MnO_x$/Au−$Si_3N_4$ and $MnO_x$/GC to the spectra of powder controls. Unlike the spectrum of $MnO_x$/GC, which has similarities to the spectrum of $Mn_2^{III}O_3$, the spectrum of $MnO_x$/Au−$Si_3N_4$ has characteristics of two different spectra corresponding to $Mn^{II}O$ and $Mn^{IV}O_2$. The $Mn^{II}O$ characteristics are established by the peak at 640 eV, a corresponding shoulder at 651 eV, and small satellite features illustrated more clearly in Figure S8, while the $Mn^{IV}O_2$ characteristics are demonstrated by the peak at 658 eV and the satellite feature approximately 12.0 eV on the high binding energy side of the $2p_{1/2}$ peak. To confirm that as-prepared $MnO_x$/Au−$Si_3N_4$ consists of two different phases, we also compare the Mn 3s spectrum of $MnO_x$/Au−$Si_3N_4$ to the spectra of $MnO_x$/GC and four powder controls in Figure 3B. We find that, in addition to gold 4f peaks, which overlap with Mn 3s features, the Mn 3s spectrum contains two separate multiplets with Δ3s values similar to those of $Mn^{II}O$ and $Mn^{IV}O_2$, providing strong evidence that the catalyst deposits as a mixture of two phases.


dx.doi.org/10.1021/ja3104632 | J. Am. Chem. Soc. 2013, 135, 8525−8534

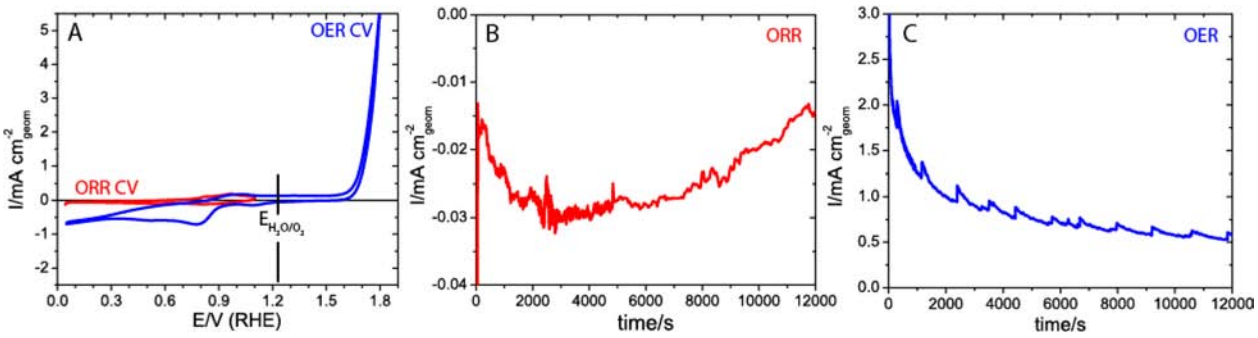


**Figure 4.** (A) Cyclic voltammetry of the catalyst performed prior to in situ XAS measurements; (B) chronoamperometry at 0.7 V during in situ XAS measurements at ORR relevant electrochemical conditions in air; (C) chronoamperometry at 1.8 V during in situ XAS measurements at OER relevant electrochemical conditions in air.

An analysis of the effect of applied potential on the surface oxidation properties of $MnO_x$/Au−$Si_3N_4$ shown in Figure 3C and D demonstrates that XPS can detect changes in the $MnO_x$/Au−$Si_3N_4$ surface after it is exposed to reaction conditions. Specifically, application of an ORR relevant potential of 0.7 V results in the elimination of $Mn^{II}O$ features and leads to $\Delta 2p_{1/2}$ and $\Delta 3s$ values that are consistent with the formation of either $Mn^{III}$ oxide or $Mn_3{}^{II,III,III}O_4$. A conclusive assignment to either phase is not possible using purely XPS because of the similarity between the $\Delta 2p_{1/2}$ and $\Delta 3s$ of $Mn_2{}^{III}O_3$ and $Mn_3{}^{II,III,III}O_4$ shown in Figure S9. Application of an OER relevant potential of 1.8 V also results in the elimination of $Mn^{II}O$ features and leads to slight changes in $\Delta 2p_{1/2}$ and $\Delta 3s$ values previously attributed to $Mn^{IV}O_2$ phase, indicating that the surface oxidation state under the OER conditions is likely a mixed valence $Mn^{III,IV}O_2$ oxide. These results provide further evidence that the $MnO_x$/Au−$Si_3N_4$ surface is unlike the surface of $MnO_x$/GC. While in both cases the oxidation state changes were expected upon exposure to the reaction conditions, these changes could not be detected with the $MnO_x$/GC catalyst using the same characterization procedure.[28] To monitor the oxidation state changes in situ and gain structural information about the catalyst both before and after exposure to reaction conditions, we performed in situ XAS experiments on a $MnO_x$/Au−$Si_3N_4$ catalyst.

**In Situ XAS under Electrochemical Reaction Conditions.** XAS data were collected using a setup illustrated in Figure 1. Prior to collecting in situ XAS measurements, cyclic voltammetry characterization of the catalyst was performed in air in ORR and OER potential windows of 0.05−1.1 V and 0.05−1.8 V. The resulting cyclic voltammetry behavior shown in Figure 4A is similar to the result obtained under standard laboratory conditions in oxygen saturated electrolyte (Figure 2A). The smaller magnitude of the ORR current obtained at beamline 10.3.2 can be explained by the smaller oxygen concentration in the air saturated electrolyte than the $O_2$ saturated electrolyte. The increase in the ORR current after exposure of the catalyst to OER potentials is attributed to the formation of oxygen bubbles on the surface of the catalyst and the resulting increase in local oxygen concentration. To acquire steady-state in situ XAS data, the $MnO_x$/Au−$Si_3N_4$ catalyst was held at an ORR relevant potential of 0.7 ± 0.007 V or at an OER relevant potential of 1.8 ± 0.001 V in 0.1 M KOH. The resulting chronoamperometry curves are shown in Figure 4B and C. The smaller instability in the potential during the OER hold and the corresponding decreased level of noise in measured current density was due to a smaller ohmic resistance during the OER experiment. The occasional drops and recovery observed in the OER chronoamperometry data were likely due to formation and disappearance of oxygen bubbles from the surface. For comparison, XAS measurements were also performed on an as-prepared (dry) catalyst.

**In Situ XANES.** In situ XANES measurements, shown in Figure 5A, follow the trend observed with ex situ XPS characterization. When the dry electrode was set in the electrochemical cell and an ORR relevant potential of 0.7 V was applied, a negative shift was observed in the XANES spectrum (Figure 5A), showing a reduction in the Mn oxidation state. On the other hand, a subsequent change to OER conditions led to a shift in the edge position to a higher energy, indicating an increase in the Mn oxidation state. Figure 5B compares the XANES spectrum obtained under the ORR conditions to the spectra of $Mn^{II}O$, $Mn_3{}^{II,III,III}O_4$, $Mn^{III}OOH$, and $\alpha$-$Mn_2{}^{III}O_3$ standards. The observed Mn valence in the catalyst during the ORR is less than 3, but greater than 2, closely matching the Mn valence of 2.7 observed in $Mn_3{}^{II,III,III}O_4$. Analysis of the $MnO_x$/Au−$Si_3N_4$ catalyst after exposure to an OER potential of 1.8 V, shown in Figure 5C, reveals that the $MnO_x$ catalyst is more oxidized than the $\alpha$-$Mn_2{}^{III}O_3$ phase, more reduced than $\beta$-$Mn^{IV}O_2$, and exhibits strong similarity to the birnessite phase. Birnessite is a naturally occurring Mn mineral with a layered structure, which accommodates cations and water in the interlayer space. Its synthetic forms, such as triclinic $Mg^{2+}$ birnessite whose spectrum is shown in Figure 5C, usually have 20−40% $Mn^{III}$ in $Mn^{IV}O_2$,[29−32] with an average oxidation state of 3.6−3.8. In addition to birnessite, the XANES spectrum of the $MnO_x$/Au−$Si_3N_4$ catalyst poised at the OER potential also shows similarities to other $Mn^{III,IV}$ oxide phases that accommodate cations into the structure (Figure S10), such as todorokite and hollandite. We will consider the birnessite phase in our subsequent analysis of the OER catalyst, as several groups have shown that birnessite can be accessed electrochemically at room temperature,[33,34] while the formation of todorokite and hollandite requires additional thermal treatment or high pressure.[32,35]

An examination of the rising edge position of $MnO_x$/Au−$Si_3N_4$ catalyst under OER condition reveals that it is slightly lower than the rising edge position of the birnessite phase, indicating that the oxidation state of the OER catalyst is approximately 3.6. The lower oxidation state in the sample than in the birnessite standard can be attributed to the contribution of some electrochemically isolated domains of $Mn_3{}^{II,III,III}O_4$ that are not oxidized under OER conditions or to a higher percentage of $Mn^{III}$ sites in the OER catalyst as compared to


dx.doi.org/10.1021/ja3104632 | J. Am. Chem. Soc. 2013, 135, 8525−8534

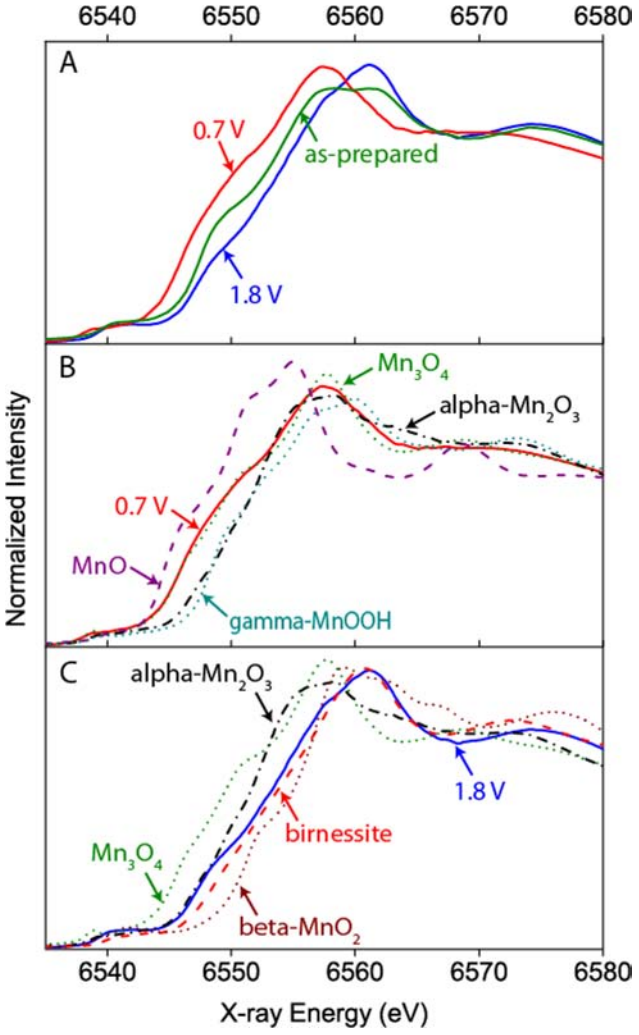


**Figure 5.** (A) Comparison of XANES data collected on as-prepared $MnO_x$/Au−$Si_3N_4$ film and on $MnO_x$/Au−$Si_3N_4$ film after in situ exposure to ORR and OER relevant conditions. (B) $MnO_x$/Au−$Si_3N_4$ film poised at 0.7 V overlaid with MnO, $Mn_3O_4$, $\alpha$-$Mn_2O_3$, and $\gamma$-MnOOH. (C) $MnO_x$/Au−$Si_3N_4$ film poised at 1.8 V overlaid with $Mn_3O_4$, $\alpha$-$Mn_2O_3$, birnessite, and $\beta$-$MnO_2$.

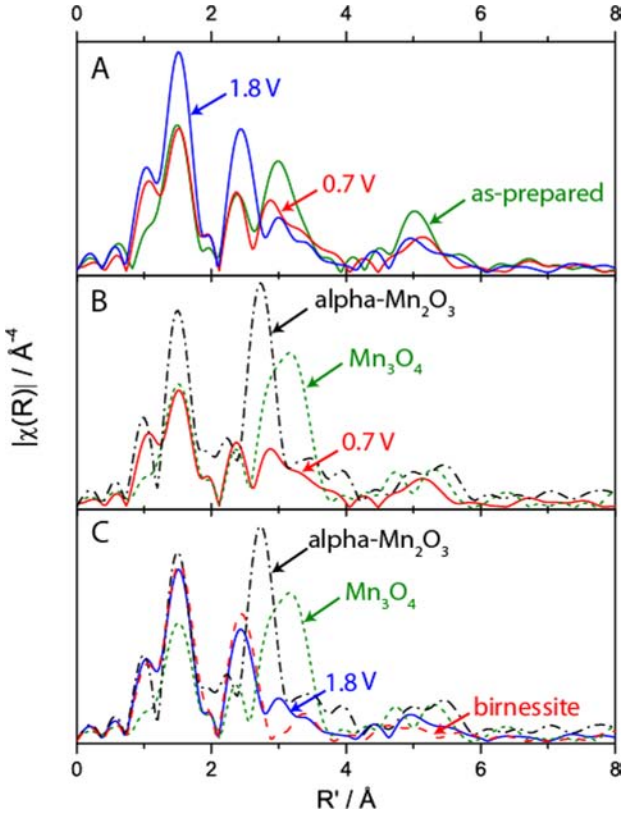


**Figure 6.** (A) Comparison of in situ EXAFS collected on as-prepared $MnO_x$/Au−$Si_3N_4$ film and on $MnO_x$/Au−$Si_3N_4$ film after in situ exposure to ORR and OER potentials. (B) $MnO_x$/Au−$Si_3N_4$ film poised at 0.7 V overlaid with $Mn_3O_4$ and $\alpha$-$Mn_2O_3$. (C) $MnO_x$/Au−$Si_3N_4$ film poised at 1.8 V overlaid with $Mn_3O_4$, $\alpha$-$Mn_2O_3$, and birnessite.

the standard. The XANES spectrum of the OER catalyst was best fit with ∼80% birnessite and ∼20% $Mn_3^{II,III,III}O_4$ spectra, although it is difficult to specify the detailed composition of the minority species (Table S3 in SI). The presence of up to 20% $Mn_3^{II,III,III}O_4$ at potentials significantly beyond the thermodynamic potential at which $Mn_3O_4$ is expected to oxidize[36] can be explained either by $Mn_3^{II,III,III}O_4$ particles electronically isolated from the rest of the sample[37] or by $Mn_3^{II,III,III}O_4$ located in the interior of the film, away from solid−liquid interface.[22] A more detailed discussion of these two possibilities is presented in the SI.

**In Situ EXAFS.** The EXAFS spectra of $MnO_x$/Au−$Si_3N_4$ shown in Figure 6A provide further information about the relevant phases. Accompanied by the oxidation state changes observed in the XANES spectra (Figure 5A), substantial changes were observed in the EXAFS spectra among as-prepared, 0.7 V, and 1.8 V $MnO_x$ samples. The presence of significant peak intensity in the R′ = 5 Å region of the as-prepared $MnO_x$ but not in the R′ = 5 Å region of 0.7 and 1.8 V samples, likely originated from the Mn−Mn−Mn multiple scattering, suggesting that the as-prepared $MnO_x$ has a more extended structure. The exact atomic arrangement in the as-prepared catalyst could not be identified because its EXAFS spectrum, which did not match any of the considered $MnO_x$ standards, likely corresponded to a mixture of $MnO_x$ phases. The presence of a mixture of phases is consistent with the results of the XPS analysis, which identified two different oxidation states on the surface of the as-prepared catalyst. EXAFS of $MnO_x$ under ORR conditions was compared with reference spectra of $Mn_3^{II,III,III}O_4$ and $\alpha$-$Mn_2^{III}O_3$ in Figure 6B. The $MnO_x$/Au−$Si_3N_4$ shows much weaker EXAFS peak intensity than the $Mn_3^{II,III,III}O_4$ in the R′ = 3 Å region, despite the similarity in the XANES region. However, the EXAFS curve fitting results show that the ORR spectrum can be fit well with the $Mn_3^{II,III,III}O_4$ atomic distances with smaller N (coordination) numbers, when the Debye−Waller factors were fixed to those of $Mn_3^{II,III,III}O_4$ (Table S4 in the SI). This can be explained by a smaller particle size as opposed to an extended crystalline material or by a distortion of the phase due to an increased amount of $Mn^{II}$ as compared to a pure $Mn_3^{II,III,III}O_4$ phase. A change to the oxidative potential of 1.8 V leads to a structural rearrangement of the $MnO_x$ catalyst and the emergence of similarities in the peak positions between the $MnO_x$ OER catalyst and a birnessite phase as shown in Figure 6C. EXAFS curve fitting of the $MnO_x$ OER catalyst was carried out using the birnessite fit result as the starting parameters (Table S4 in the SI). This approach generated a good fit, but required smaller N values than those found for the reference birnessite compound. The smaller N values indicate the


dx.doi.org/10.1021/ja3104632 | J. Am. Chem. Soc. 2013, 135, 8525−8534

presence of nondiffracting, small particle domains as opposed to an extended crystalline material and suggest the presence of a minority phase, such as $Mn_3^{II,III,III}O_4$, in agreement with the XANES analysis. We note that, based purely on EXAFS spectra, a todorokite tunnel structure could have also generated a good fit.[7,38] As mentioned in the discussion of XANES, however, we considered the birnessite phase in our analysis because it can form electrochemically,[33,34] while the formation of todorokite requires an additional high temperature treatment.[32]

**In Situ XANES To Assess Film Porosity.** To understand if OER catalysis is limited to the top geometric layer of a dense film, or if it occurs throughout the catalyst layer of a porous film, we prepared a second $MnO_x$/Au−$Si_3N_4$ catalyst. The catalyst was synthesized by reducing the number of deposition cycles from nine to one, yielding a sample half as thick as measured using cross-sectional scanning electron microscopy (SEM), Figure 7A and B. Despite the factor of 2 difference in film thickness, the samples exhibit similar XANES spectra under both the ORR and the OER conditions (Figure 7C). As the spectra were collected by fluorescence, providing information on the entirety of these relatively thin films, the similarity in the spectra suggests that the catalytic film is porous enough for both samples to have the same fraction of the electrochemically accessible material, as illustrated in Figure 8. A comparison of the OER current at 1.8 V, presented in Figure 7D, reveals about a factor of 2 higher current for the thicker sample, indicating a direct relationship between the thickness of the catalytic film and the OER activity. This result provides further evidence that the catalyst film is highly porous, allowing the reaction to occur throughout the entire catalyst structure. In this structure, we expect the more oxidized $Mn^{III,IV}$ oxide to be in contact with electrolyte and participate in OER, and the more reduced $Mn_3^{II,III,III}O_4$ to be located in the interior of the catalyst, away from the solid−liquid interface, with no opportunity to participate in electrocatalysis. It is also possible, however, that $Mn_3^{II,III,III}O_4$ may remain unoxidized at the surface of the catalyst, due to poor contact between $Mn_3^{II,III,III}O_4$ particles and the rest of the film, as discussed in the SI. Because the electronically isolated $Mn_3^{II,III,III}O_4$ would also be unable to participate in OER electrocatalysis, we can link the oxidized $Mn^{III,IV}$ oxide to the observed OER current.

**Analysis of $K^+$ Intercalation.** Because birnessite $MnO_x$ has layered structure that accommodates ions, it was important to consider potassium intercalation into the catalyst during the characterization in potassium hydroxide electrolyte. Previously, potassium intercalation into $MnO_x$ has been reported both under ORR[39,40] and OER conditions.[41,42] A recent study has also demonstrated that potassium may have a favorable effect on OER by stabilizing the layered structure of $MnO_x$.[43] To monitor possible intercalation we used ex situ XPS measurements, which provided the ratio of potassium to Mn on the surface of the $MnO_x$/Au−$Si_3N_4$ catalyst after its exposure to 0.7 and 1.8 V. Measurements were also performed on the as-prepared catalyst, in which no potassium cations could be present. Our results, shown in Figure S11, indicate that a small amount of potassium, corresponding to one $K^+$ for every hundred Mn, intercalates into the catalyst after exposure to the OER conditions, while intercalation under ORR conditions is negligible. This amount is less than what is expected for the synthetic birnessites,[29,30,32] indicating that the $MnO_x$/Au−$Si_3N_4$ catalyst under the OER conditions is composed of Mn sites with and without intercalated $K^+$. Further investigation is necessary to determine the role of $K^+$ in OER catalysis.

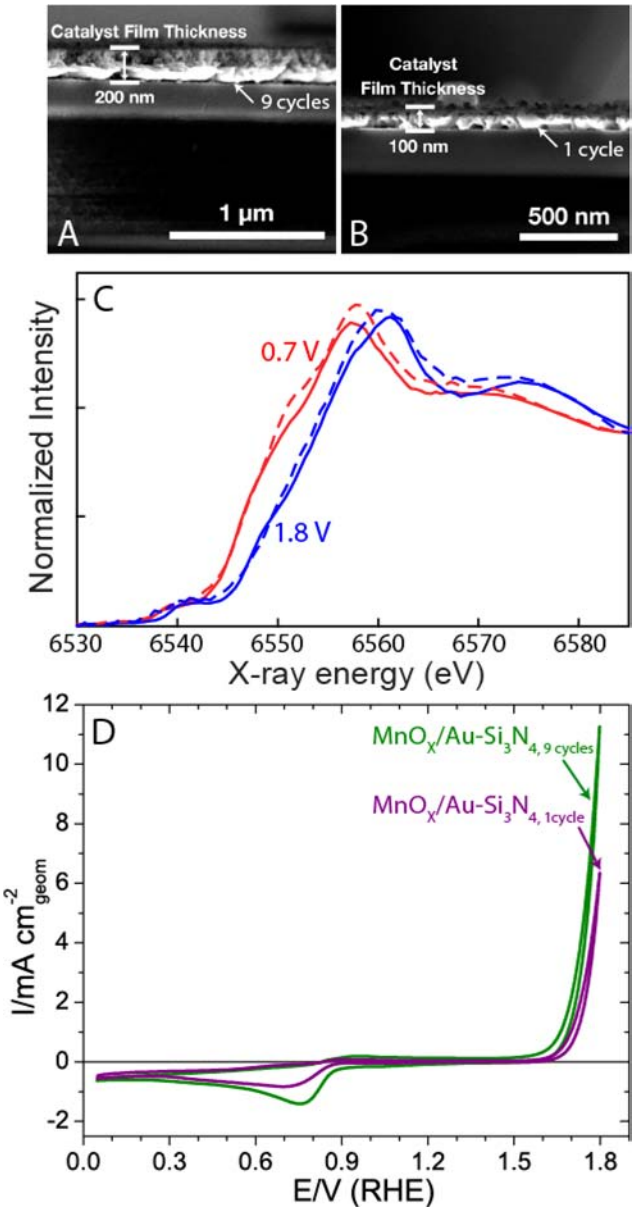


**Figure 7.** (A) Scanning electron microscopy (SEM) image of 200 nm $MnO_x$ on Au−$Si_3N_4$ after 9 cyclic voltammetry (CV) cycles of deposition. (B) SEM image of 100 nm $MnO_x$ on $AuSi_3N_4$, demonstrating a 2-fold reduction in the thickness of $MnO_x$ after the number of CV deposition cycles is lowered from 9 to 1. (C) Comparison of XANES for 9 (solid lines) and 1 (dashed lines) cycle samples after exposure to ORR (red) and OER (blue) potentials. (D) CV characterization of the ORR and the OER activities, illustrating that the OER activity scales with the thickness of $MnO_x$ catalyst.

**Structural Transformations as a Function of Applied Potential.** The in situ XAS characterization of the $MnO_x$/Au−$Si_3N_4$ catalyst identified a structural transformation of the catalyst with changes in the applied potential. These results indicate that different phases form under the ORR and OER conditions. ORR potentials favor the formation of a disordered $Mn_3^{II,III,III}O_4$ phase with a spinel-like structure shown in Figure 9A, while the OER potentials favor the formation of an oxidized $MnO_x$ phase, bearing similarities to birnessite structure shown in Figure 9B, along with a less oxidized phase, likely corresponding to unchanged $Mn_3^{II,III,III}O_4$.


dx.doi.org/10.1021/ja3104632 | J. Am. Chem. Soc. 2013, 135, 8525−8534

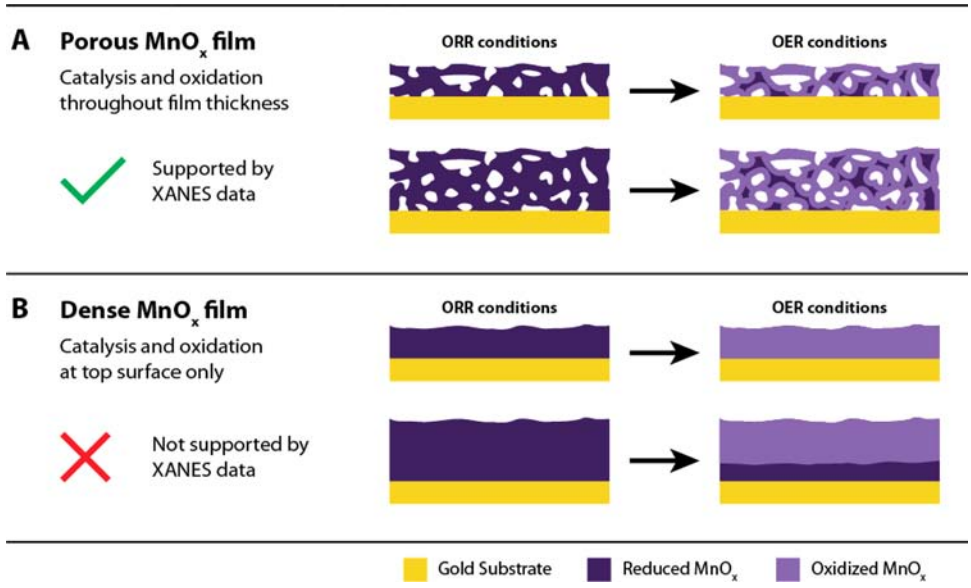


**Figure 8.** (A) Schematic of oxidation within a porous thin film, illustrating the same ratio of oxidized to reduced $MnO_x$ for both thick and thin catalytic layers. (B) Schematic of oxidation within a dense thin film, illustrating a higher ratio of oxidized to reduced $MnO_x$ for a thinner film. The porous structure is consistent with XANES measurements presented in Figure 6C.

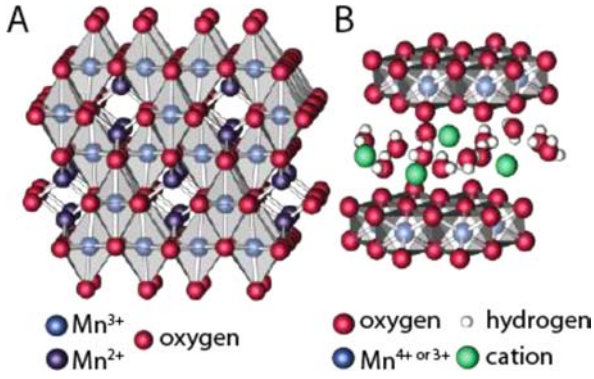


**Figure 9.** Schematic showing the crystal structures of (A) $Mn_3O_4$, which consists of octahedral (light blue) and tetragonal (dark blue) Mn sites, and (B) $M^{n+}$-birnessite, which consists of sheets of edge-sharing $MnO_6$ octahedra with cations and water intercatalated into the interlayer space.

The presence of a highly disordered $Mn_3^{II,III,III}O_4$ phase at 0.7 V links $Mn_3^{II,III,III}O_4$ to the high activity for the ORR. The formation of the $Mn_3^{II,III,III}O_4$ phase at 0.7 V is expected based on thermodynamics,[36,44] but experiments show that this phase is not very kinetically accessible. Specifically, in base, the reduction of $Mn^{IV}O_2$ to $Mn_3^{II,III,III}O_4$ has been previously demonstrated only in highly concentrated KOH electrolytes[45,46] and has been characterized by poor electrochemical reversibility and conductivity.[45,47,48] Mechanistic studies in low concentration KOH electrolytes by Kozawa and Yeager, more applicable to the present investigation, have identified Mn(III) oxide as the final reduction product of $Mn^{IV}O_2$.[46] In situ XAS characterization by Lima et al. of another ORR catalyst consisting of $MnO_x$ dispersed in Vulcan carbon detected the presence of some $Mn_3^{II,III,III}O_4$ at a similar cathodic potential during the cathodic sweep, but in a mixture with a more oxidized Mn(III) phase, likely corresponding to $Mn^{III}OOH$.[4] The scarcity of reports of complete reduction of $MnO_x$ to $Mn_3^{II,III,III}O_4$ under potentials relevant for ORR at pH 13 warrants further investigation of the reductive behavior of $MnO_x/Au-Si_3N_4$ and identification of the precise voltage at which the phase transition to $Mn_3^{II,III,III}O_4$ begins.

Electrochemical oxidation of the $Mn_3^{II,III,III}O_4$ phase to a phase similar to birnessite is not expected based on the early studies of $MnO_x$ as battery electrodes, which have suggested that $Mn_3^{II,III,III}O_4$ is electrochemically inactive and cannot be oxidized.[4,45,47−49] Recent studies of $MnO_x$ supercapacitors, however, have not only identified $Mn_3^{II,III,III}O_4$ as a phase with excellent electrochemical conductivity and redox properties[50−53] but have also shown that it can transform into a layered structure of birnessite after 100−1000 electrochemical cycles.[33,34,54] The ability of our catalyst to transform from the $Mn_3^{II,III,III}O_4$ phase formed at 0.7 V to greater than 80% of birnessite-like phase after a single cycle to an OER relevant potential of 1.8 V is likely explained by the small domain size of the crystallites in the catalyst and the disordered structure of the starting $Mn_3^{II,III,III}O_4$ phase. Our study provides the first evidence of the formation of $MnO_x$ with a birnessite-like structure during the OER in alkaline environment. Considering that previous studies have also linked a mixed $Mn^{III,IV}$ oxide phase with similarities to birnessite to high OER activity in acidic nafion membrane[7] and neutral electrolytes,[16,55,56] our results suggest that the OER activity of the mixed $Mn^{III,IV}$ oxide may be independent of the pH environment. Further studies are necessary to determine the exact active site and the reaction mechanism.

## ■ CONCLUSIONS

Identifying the active sites in catalysis, one of the most challenging endeavors to undertake in the field, is critical to understanding and improving catalytic materials. In situ X-ray absorption spectroscopy (XAS) studies were employed to investigate the active phases of a manganese oxide ($MnO_x$) catalyst supported onto $Au-Si_3N_4$ ($MnO_x/Au-Si_3N_4$) during electrochemical reaction conditions for the oxygen reduction reaction (ORR) and the oxygen evolution reaction (OER). The investigations identified a disordered $Mn_3^{II,III,III}O_4$ as a phase under ORR conditions, and a mixture of two $MnO_x$ phases


dx.doi.org/10.1021/ja3104632 | J. Am. Chem. Soc. 2013, 135, 8525−8534

under OER conditions: an oxidized phase with a structure similar to that of birnessite and a more reduced phase, likely corresponding to unchanged $Mn_3^{II,III,III}O_4$. By studying catalyst films of different thicknesses, it was shown that OER catalysis must occur throughout the catalyst structure and not just at the topmost geometric layer of the film, indicating excellent porosity of the films. Although we identify a mixture of a more oxidized phase and $Mn_3^{II,III,III}O_4$ under OER conditions, due to the oxidizing potentials necessary for the OER we expect the more reduced $Mn_3^{II,III,III}O_4$ to be located away from the solid−liquid interface with no opportunity to turn over the reaction and the more oxidized phase to be in contact with the electrolyte and be important to the observed OER catalysis. As the electrochemical properties of $MnO_x$ are highly dependent on the starting $MnO_x$ phase[45,57] and underlying support, it is important to continue in situ investigations of different $MnO_x$ materials under ORR and OER conditions to advance understanding of the structural parameters and surface conditions that contribute to the high activity observed for the two reactions.

## ■ ASSOCIATED CONTENT

### Ⓢ Supporting Information

X-ray photoelectron spectroscopy analysis, X-ray absorption spectroscopy fitting details, Figures S1−S8. This material is available free of charge via the Internet at http://pubs.acs.org.

## ■ AUTHOR INFORMATION


### Corresponding Author

jyano@lbl.gov; jaramillo@stanford.edu

### Present Address

B.L.-K.: Synchrotron SOLEIL, L'Orme des Merisiers, BP 42 Saint-Aubin 91192, Gif-sur-Yvette, France.


### Author Contributions

Y.G. and B.L.-K. contributed equally.

### Notes

The authors declare no competing financial interest.

## ■ ACKNOWLEDGMENTS

Catalyst development and electrochemical characterization were supported as part of the Center on Nanostructuring for Efficient Energy Conversion (CNEEC) at Stanford University, an Energy Frontier Research Center funded by the U.S. Department of Energy, Office of Science, Office of Basic Energy Sciences under Award Number DE-SC0001060. SEM, XPS, and XRD were performed at the Stanford Nanocharacterization Laboratory (SNL) part of the Stanford Nano Shared Facilities. In situ XAS experiments were supported by the Joint Center for Artificial Photosynthesis, a DOE Energy Innovation Hub, supported through the Office of Science of the U.S. Department of Energy under Award Number DE-SC0004993, and performed at the Advanced Light Source (BL 10.3.2), Berkeley, under Contract DE-AC02-05CH11231. Portions of this research were carried out at the Stanford Synchrotron Radiation Lightsource, a Directorate of SLAC National Accelerator Laboratory and an Office of Science User Facility operated for the U.S. Department of Energy Office of Science by Stanford University. The SSRL Structural Molecular Biology Program is supported by the DOE Office of Biological and Environmental Research, and by the National Institutes of Health, National Institute of General Medical Sciences (including P41GM103393), and the National Center for Research Resources (P41RR001209). The authors thank Dr. Sung-Hyeon Baeck for providing beta-$MnO_2$ and $\alpha$-$Mn_2O_3$ powders and Dr. Jakob Kibsgaard for assistance with Figure 9.

## ■ REFERENCES


(1) Peuckert, M.; Yoneda, T.; Betta, R. A. D.; Boudart, M. *J. Electrochem. Soc.* **1986**, *133*, 944.
(2) Mukerjee, S.; Srinivasan, S.; Soriaga, M. P.; McBreen, J. *J. Electrochem. Soc.* **1995**, *142*, 1409.
(3) Lima, F. H. B.; Calegaro, M. L.; Ticianelli, E. A. *J. Electroanal. Chem.* **2006**, *590*, 152.
(4) Lima, F. H. B.; Calegaro, M. L.; Ticianelli, E. A. *Electrochim. Acta* **2007**, *52*, 3732.
(5) Kanan, M. W.; Yano, J.; Surendranath, Y.; Dinca, M.; Yachandra, V. K.; Nocera, D. G. *J. Am. Chem. Soc.* **2010**, *132*, 13692.
(6) Bediako, D. K.; Lassalle-Kaiser, B.; Surendranath, Y.; Yano, J.; Yachandra, V. K.; Nocera, D. G. *J. Am. Chem. Soc.* **2012**, *134*, 6801.
(7) Hocking, R. K.; Brimblecombe, R.; Chang, L. Y.; Singh, A.; Cheah, M. H.; Glover, C.; Casey, W. H.; Spiccia, L. *Nat. Chem.* **2011**, *3*, 461.
(8) Haas, O.; Holzer, F.; Müller, S.; McBreen, J. M.; Yang, X. Q.; Sun, X.; Balasubramanian, M. *Electrochim. Acta* **2002**, *47*, 3211.
(9) Yeager, E. *J. Mol. Catal.* **1986**, *38*, 5.
(10) Mao, L. Q.; Sotomura, T.; Nakatsu, K.; Koshiba, N.; Zhang, D.; Ohsaka, T. *J. Electrochem. Soc.* **2002**, *149*, A504.
(11) Cao, Y. L.; Yang, H. X.; Ai, X. P.; Xiao, L. F. *J. Electroanal. Chem.* **2003**, *557*, 127.
(12) Cheng, F. Y.; Su, Y.; Liang, J.; Tao, Z. L.; Chen, J. *Chem. Mater.* **2010**, *22*, 898.
(13) Gorlin, Y.; Jaramillo, T. F. *J. Am. Chem. Soc.* **2010**, *132*, 13612.
(14) Morita, M.; Iwakura, C.; Tamura, H. *Electrochim. Acta* **1979**, *24*, 357.
(15) El-Deab, M. S.; Awad, M. I.; Mohammad, A. M.; Ohsaka, T. *Electrochem. Commun.* **2007**, *9*, 2082.
(16) Zaharieva, I.; Najafpour, M. M.; Wiechen, M.; Haumann, M.; Kurz, P.; Dau, H. *Energy Environ. Sci.* **2011**, *4*, 2400.
(17) Tench, D.; Warren, L. F. *J. Electrochem. Soc.* **1983**, *130*, 869.
(18) Gilbert, B.; Frazer, B. H.; Belz, A.; Conrad, P. G.; Nealson, K. H.; Haskel, D.; Lang, J. C.; Srajer, G.; De Stasio, G. *J. Phys. Chem. A* **2003**, *107*, 2839.
(19) Barr, T. L.; Seal, S. *J. Vac. Sci. Technol., A* **1995**, *13*, 1239.
(20) Dicastro, V.; Polzonetti, G. *J. Electron Spectrosc. Relat. Phenom.* **1989**, *48*, 117.
(21) Oku, M.; Hirokawa, K.; Ikeda, S. *J. Electron Spectrosc. Relat. Phenom.* **1975**, *7*, 465.
(22) Djurfors, B.; Broughton, J. N.; Brett, M. J.; Ivey, D. G. *J. Electrochem. Soc.* **2006**, *153*, A64.
(23) Marcus, M. A.; MacDowell, A. A.; Celestre, R.; Manceau, A.; Miller, T.; Padmore, H. A.; Sublett, R. E. *J. Synchrotron Radiat.* **2004**, *11*, 239.
(24) Newville, M. *J. Synchrotron Radiat.* **2001**, *8*, 96.
(25) Rehr, J. J.; Albers, R. C. *Rev. Mod. Phys.* **2000**, *72*, 621.
(26) Webb, S. M.; Tebo, B. M.; Bargar, J. R. *Am. Mineral.* **2005**, *90*, 1342.
(27) Burke, L. D.; Osullivan, J. F. *Electrochim. Acta* **1992**, *37*, 585.
(28) Gorlin, Y.; Jaramillo, T. F. *J. Electrochem. Soc.* **2012**, *159*, H782.
(29) Post, J. E.; Heaney, P. J.; Hanson, J. *Powder Diffr.* **2002**, *17*, 218.
(30) Post, J. E.; Veblen, D. R. *Am. Mineral.* **1990**, *75*, 477.
(31) Ching, S.; Petrovay, D. J.; Jorgensen, M. L.; Suib, S. L. *Inorg. Chem.* **1997**, *36*, 883.
(32) Golden, D. C.; Chen, C. C.; Dixon, J. B. *Clays Clay Miner.* **1987**, *35*, 271.
(33) Dubal, D. P.; Jagadale, A. D.; Lokhande, C. D. *Electrochim. Acta* **2012**, *80*, 160.
(34) Dai, Y.; Wang, K.; Xie, J. *Appl. Phys. Lett.* **2007**, *90*, 104102.
(35) Shen, Y. F.; Zerger, R. P.; DeGuzman, R. N.; Suib, S. L.; McCurdy, L.; Potter, D. I.; O'Young, C. L. *Science* **1993**, *260*, 511.

(36) Pourbaix, M. *Atlas of Electrochemical Equilibria in Aqueous Solutions*; Pergamon Press: Elmsford, NY, 1966.
(37) Lowe, M. A.; Gao, J.; Abruna, H. D. *J. Mater. Chem. A* **2013**, *1*, 2094.
(38) Manceau, A.; Gorshkov, A. I.; Drits, V. A. *Am. Mineral.* **1992**, *77*, 1144.
(39) Minakshi, M. *J. Electroanal. Chem.* **2008**, *616*, 99.
(40) Athouel, L.; Moser, F.; Dugas, R.; Crosnier, O.; Belanger, D.; Brousse, T. *J. Phys. Chem. C* **2008**, *112*, 7270.
(41) Chigane, M.; Ishikawa, M. *J. Electrochem. Soc.* **2000**, *147*, 2246.
(42) Chigane, M.; Ishikawa, M. *J. Chem. Soc., Faraday Trans.* **1998**, *94*, 3665.
(43) Boppana, V. B. R.; Yusuf, S.; Hutchings, G. S.; Jiao, F. *Adv. Funct. Mater.* **2013**, *23*, 878.
(44) Su, H.-Y.; Gorlin, Y.; Man, I. C.; Calle-Vallejo, F.; Norskov, J. K.; Jaramillo, T. F.; Rossmeisl, J. *Phys. Chem. Chem. Phys.* **2012**, *14*, 14010.
(45) McBreen, J. *Electrochim. Acta* **1975**, *20*, 221.
(46) Kozawa, A.; Yeager, J. F. *J. Electrochem. Soc.* **1965**, *112*, 959.
(47) Boden, D.; Venuto, C. J.; Wisler, D.; Wylie, R. B. *J. Electrochem. Soc.* **1967**, *114*, 415.
(48) Boden, D.; Venuto, C. J.; Wisler, D.; Wylie, R. B. *J. Electrochem. Soc.* **1968**, *115*, 333.
(49) Nam, K. W.; Kim, M. G.; Kim, K. B. *J. Phys. Chem. C* **2007**, *111*, 749.
(50) Jiang, J.; Kucernak, A. *Electrochim. Acta* **2002**, *47*, 2381.
(51) Djurfors, B.; Broughton, J. N.; Brett, M. J.; Ivey, D. G. *J. Mater. Sci.* **2003**, *38*, 4817.
(52) Zhang, F.; Zhang, X.-G.; Hao, L. *Mater. Chem. Phys.* **2011**, *126*, 853.
(53) Lin, Y.-H.; Wei, T.-Y.; Chien, H.-C.; Lu, S.-Y. *Adv. Eng. Mater.* **2011**, *1*, 901.
(54) Dubal, D. P.; Dhawale, D. S.; Salunkhe, R. R.; Lokhande, C. D. *J. Electroanal. Chem.* **2010**, *647*, 60.
(55) Zaharieva, I.; Chernev, P.; Risch, M.; Klingan, K.; Kohlhoff, M.; Fischer, A.; Dau, H. *Energy Environ. Sci.* **2012**, *5*, 7081.
(56) Iyer, A.; Del-Pilar, J.; King'ondu, C. K.; Kissel, E.; Garces, H. F.; Huang, H.; El-Sawy, A. M.; Dutta, P. K.; Suib, S. L. *J. Phys. Chem. C* **2012**, *116*, 6474.
(57) Desai, B. D.; Fernandes, J. B.; Dalal, V. N. K. *J. Power Sources* **1985**, *16*, 1.